

Non-Oscillatory Central Difference and Artificial Viscosity Schemes for Relativistic Hydrodynamics

Peter Anninos and P. Chris Fragile

University of California, Lawrence Livermore National Laboratory, Livermore CA 94550

ABSTRACT

High resolution, non-oscillatory, central difference (NOCD) numerical schemes are introduced as alternatives to more traditional artificial viscosity (AV) and Godunov methods for solving the fully general relativistic hydrodynamics equations. These new approaches provide the advantages of Godunov methods in capturing ultra-relativistic flows without the cost and complication of Riemann solvers, and the advantages of AV methods in their speed, ease of implementation, and general applicability without explicitly using artificial viscosity for shock capturing. Shock tube, wall shock, and dust accretion tests are presented and compared against equivalent solutions from both AV and Godunov based codes. In the process we address the accuracy of time-explicit NOCD and AV methods over a wide range of Lorentz factors.

Subject headings: gravitation — hydrodynamics — relativity — methods: numerical

1. Introduction

The earliest attempts at simulating relativistic flows in the presence of strong gravitational fields are attributed to May and White (1966, 1967) who investigated gravitational collapse in a one dimensional Lagrangian code using artificial viscosity (AV) methods (Von-Neumann & Richtmyer 1950) to capture shock waves. Wilson (1972, 1979) subsequently introduced an alternative Eulerian coordinate approach in multi-dimensional calculations, using traditional finite difference upwind methods and artificial viscosity for shock capturing. Since these earliest studies, AV methods have continued to be developed in their popularity and applied to a variety of problems due largely to their general robustness (Hawley, Smarr, & Wilson 1984a,b; Centrella & Wilson 1984; Anninos 1998). These methods are also computationally cheap, easy to implement, and easily adaptable to multi-physics applications. However, it has been demonstrated that problems involving high Lorentz factors (greater

than a few) are particularly sensitive to different implementations of the viscosity terms, and can result in large numerical errors if solved using time explicit methods (Norman & Winkler 1986).

Significant progress has been made in recent years to take advantage of the conservational form of the hydrodynamics system of equations to apply Godunov-type methods and approximate Riemann solvers to simulate ultra-relativistic flows (Eulderink & Mellema 1995; Banyuls et al. 1997; Font et al. 2000). Although Godunov-based schemes are accepted as more accurate alternatives to AV methods, especially in the limit of high Lorentz factors, they are not infallible and should generally be used with caution. They may produce unexpected results in certain cases that can be overcome only with specialized fixes or by adding additional dissipation. A few known examples include the admittance of expansion shocks, negative internal energies in kinematically dominated flows, ‘carbuncle’ effect in high Mach number bow shocks, kinked Mach stems, and odd/even decoupling in mesh-aligned shocks (Quirk 1994). Godunov methods, whether they solve the Riemann problem exactly or approximately, are also computationally much more expensive than their simpler AV counterparts, and more difficult to extend the system of equations to include additional physics.

Hence we have undertaken this current study to explore an alternative approach of using high resolution, non-oscillatory, central difference (NOCN) methods (Jiang et al. 1998; Jiang & Tadmor 1998) to solve the relativistic hydrodynamics equations. These new schemes combine the speed, efficiency, and flexibility of AV methods with the advantages of the potentially more accurate conservative formulation approach of Godunov methods, but without the cost and complication of Riemann solvers and flux splitting.

The NOCN methods are implemented as part of a new code we developed called Cosmos, and designed for fully general relativistic problems. Cosmos is a collection of massively parallel, multi-dimensional, multi-physics solvers applicable to both Newtonian and general relativistic systems, and currently includes five different computational fluid dynamics (CFD) methods, equilibrium and non-equilibrium primordial chemistry, photoionization, radiative cooling, radiation flux-limited diffusion, radiation pressure, scalar fields, Newtonian external and self gravity, arbitrary spacetime geometries, and viscous stress. The five hydrodynamics methods include a Godunov (TVD) solver for Newtonian flows, two artificial viscosity codes for general relativistic systems (differentiated by mesh or variable centering type: staggered versus zone-centered), and two relativistic methods based on non-oscillatory central difference schemes (differentiated also by the mesh type: staggered versus centered in time and space). The emphasis in the following sections is to review our particular implementations of the AV and NOCN methods and compare results of various shock wave and accretion

test calculations with other published results. We also explore the accuracy of both AV and NOCD methods in simulating ultra-relativistic shocks over a wide range of Lorentz factors.

2. Basic Equations

2.1. Internal Energy Formulation

Both of the artificial viscosity methods in Cosmos are based on an internal energy formulation of the perfect fluid conservation equations. The equations are derived from the 4-velocity normalization $u^\mu u_\mu = -1$, the conservation of baryon number $\nabla_\mu(\rho u^\mu) = 0$ for the fluid rest mass density, the parallel component of the stress–energy conservation equation $u_\nu \nabla_\mu T^{\mu\nu} = 0$ for internal energy, the transverse component of the stress–energy conservation equation $(g_{\alpha\nu} + u_\alpha u_\nu) \nabla_\mu T^{\mu\nu} = 0$ for momentum, and an equation of state (eos) for the fluid pressure $P = P(\rho, \epsilon)$, which for an ideal gas is $P = (\Gamma - 1)e$, where Γ is the adiabatic index and e is the fluid internal energy density. For a perfect fluid, the stress-energy tensor is

$$T^{\mu\nu} = \rho h u^\mu u^\nu + P g^{\mu\nu}, \quad (2-1)$$

where

$$h = 1 + \epsilon + \frac{P}{\rho} = 1 + \Gamma \epsilon \quad (2-2)$$

is the relativistic enthalpy, ϵ is the specific internal energy, u^μ is the contravariant 4-velocity, and $g_{\mu\nu}$ is the 4-metric. The resulting equations can be written in flux conservative form as (Wilson 1979)

$$\frac{\partial D}{\partial t} + \frac{\partial(DV^i)}{\partial x^i} = 0, \quad (2-3)$$

$$\frac{\partial E}{\partial t} + \frac{\partial(EV^i)}{\partial x^i} + P \frac{\partial W}{\partial t} + P \frac{\partial(WV^i)}{\partial x^i} = 0 \quad (2-4)$$

$$\frac{\partial S_j}{\partial t} + \frac{\partial(S_j V^i)}{\partial x^i} - \frac{S^\mu S^\nu}{2S^0} \frac{\partial g_{\mu\nu}}{\partial x^j} + \sqrt{-g} \frac{\partial P}{\partial x^j} = 0, \quad (2-5)$$

where g is the determinant of the 4-metric, $W = \sqrt{-g} u^0$ is the relativistic boost factor, $D = W\rho$ is the generalized fluid density, $V^i = u^i/u^0$ is the transport velocity, $S_i = W\rho h u_i$ is the covariant momentum density, and $E = We = W\rho\epsilon$ is the generalized internal energy density. We use the standard convention in which Greek (Latin) indices refer to 4(3)-space components.

The system of equations (2-3) – (2-5) are complemented by two additional expressions for V^i and W that are convenient for numerical computation. Introducing a general tensor

form for artificial viscosity Q_{ij} (see section 3.1), and defining

$$M = \rho h W = \rho h \sqrt{-g} u^0 = E + D + (P + \text{tr}[Q_{ij}])W, \quad (2-6)$$

the momentum can be expressed as $S_\mu = M u_\mu$, and S_0 is computed from the normalization of the four-velocity $S^\mu S_\mu = -M^2$. The coordinate velocity then becomes $V^i = S^i/S^0$ with $V^0 = 1$. Also, the time component of the four-velocity u^0 can be calculated from the normalization $u_\mu u^\mu = u^0 V^\mu S_\mu / M = -1$, and used to derive the following expressions for W

$$W = \frac{-\sqrt{-g} M}{S_\mu V^\mu} = \frac{\sqrt{-g} S^0}{\rho h W}. \quad (2-7)$$

The former expression ($W = -\sqrt{-g} M / (S_\mu V^\mu)$) is used in the staggered mesh AV schemes as it results in more accurate density and velocity jump conditions across shock fronts. The latter is more convenient for the zone centered NOCD methods.

2.2. Conservative Energy Formulation

The second class of numerical methods presented in this paper (the NOCD schemes) are based on a simpler conservative hyperbolic formulation of the hydrodynamics equations. In this case, the equations are derived directly from the conservation of stress-energy

$$\nabla_\mu T^{\mu\nu} = \frac{1}{\sqrt{-g}} (\sqrt{-g} T^{\mu\nu})_{,\mu} + \Gamma_{\alpha\mu}^\nu T^{\mu\alpha} = 0. \quad (2-8)$$

Expanding (2-8) into time and space explicit parts yields the flux conservative equations for general stress-energy tensors

$$\frac{\partial(\sqrt{-g} T^{0\nu})}{\partial t} + \frac{\partial(\sqrt{-g} T^{i\nu})}{\partial x^i} = \Sigma^\nu, \quad (2-9)$$

with curvature source terms

$$\Sigma^\nu = -\sqrt{-g} T^{\beta\gamma} \Gamma_{\beta\gamma}^\nu. \quad (2-10)$$

Substituting the perfect fluid stress tensor (2-1) into (2-9), and including baryon conservation results in the following set of equations

$$\frac{\partial D}{\partial t} + \frac{\partial(DV^i)}{\partial x^i} = 0, \quad (2-11)$$

$$\frac{\partial \mathcal{E}}{\partial t} + \frac{\partial(\mathcal{E}V^i)}{\partial x^i} + \frac{\partial[\sqrt{-g} (g^{0i} - g^{00}V^i) P]}{\partial x^i} = \Sigma^0, \quad (2-12)$$

$$\frac{\partial \mathcal{S}^j}{\partial t} + \frac{\partial(\mathcal{S}^j V^i)}{\partial x^i} + \frac{\partial[\sqrt{-g} (g^{ij} - g^{0j}V^i) P]}{\partial x^i} = \Sigma^j, \quad (2-13)$$

where the variables D , V^i , and g are the same as those defined in the internal energy formulation. However, now

$$\mathcal{E} = W \rho h u^0 + \sqrt{-g} g^{00} P, \quad (2-14)$$

$$\mathcal{S}^i = W \rho h u^i + \sqrt{-g} g^{0i} P, \quad (2-15)$$

are the new expressions for energy and momenta.

It is convenient to express \mathcal{E} and \mathcal{S}^i in terms of the internal energy formulation variables, especially for initializing data

$$\mathcal{E} = \frac{W^2}{\sqrt{-g}} \left(\frac{D}{W} + \Gamma \frac{E}{W} \right) + (\Gamma - 1) \sqrt{-g} g^{00} \frac{E}{W}, \quad (2-16)$$

$$\mathcal{S}^i = g^{i\alpha} S_\alpha + (\Gamma - 1) \sqrt{-g} g^{0i} \frac{E}{W}, \quad (2-17)$$

and reconstructing the equation of state

$$P = (\Gamma - 1) \frac{E}{W} \quad (2-18)$$

$$= \left(\frac{\mathcal{E} \sqrt{-g}}{W^2} - \frac{D}{W} \right) \frac{\Gamma - 1}{\Gamma + (\Gamma - 1) g^{00} (\sqrt{-g}/W)^2}, \quad (2-19)$$

where we have explicitly assumed an adiabatic gamma-law fluid.

3. Numerical Methods

Cosmos is a multi-dimensional (1, 2 or 3D) code that uses regularly spaced Cartesian meshes for spatial finite differencing or finite volume discretization methods. Evolved variables are defined at the zone centers in the NOCD, TVD, and non-staggered AV methods. In the staggered mesh AV method, variables are centered either at zone faces (the velocity V^j and momentum S_j vectors) or zone centers (all other scalar and tensor variables). Periodic, reflection, constant in time, user-specified, and flat (vanishing first derivative) boundary conditions are supported for all variables in the evolutions. The hydrodynamic equations in both of the formalisms presented in §2 are solved with time-explicit, operator split methods with second order spatial finite differencing. Single-step time integration and dimensional splitting is used for both AV methods. The NOCD schemes use a second order predictor-corrector time integration with dimensional splitting, and the TVD approach utilizes a third order Runge-Kutta time integration with finite volume representations for source updates. Since the main emphasis here is on relativistic hydrodynamics, the following discussion is limited to presenting details relevant for the AV and NOCD schemes: the TVD method is currently only Newtonian.

3.1. Artificial Viscosity

The order and frequency in which various source terms and state variables are updated in the AV methods can affect the numerical accuracy, especially in high boost flows. The following order composing a complete single cycle or timestep solution has been determined to produce a reasonable compromise between cost and accuracy:

- Compute timestep Δt from (3-1)
- Store current value of boost factor W
- Curvature
 - compute pressure and sound speed from the ideal fluid equation of state:
 $P = (\Gamma - 1)E/W$, $C_s = \sqrt{\Gamma P/(\rho h)}$
 - evaluate scalar or tensor artificial viscosity Q_{ij}
 - normalize velocity and update boost factor:
 $V^i = S^i/S^0$, using $S_\mu S^\mu = -M^2 = -(D + E + PW + \text{tr}[Q_{ij}]W)^2$ to first compute S_0 ;
 then construct S^μ from $g^{\mu\nu}$, S_0 , and the evolved S_j ;
 and finally use equation (2-7) to define the boost factor $W = -\sqrt{-g}M/(S_\mu V^\mu)$
 - update momentum, accounting for curvature:
 $\dot{S}_j = S^\mu S^\nu g_{\mu\nu,j}/(2S^0)$, using second order finite differencing of $g_{\mu\nu}$
- Artificial viscosity
 - compute pressure
 - normalize velocity, update W
 - compute pressure and sound speed
 - evaluate artificial viscosity components Q_{ij}
 - update momentum and energy equations accounting for Q_{ij} :
 $\dot{E} = -\sum_{i,j} Q_{ij}[\nabla_i(WV^j) + \nabla_j(WV^i)]/2$, and $\dot{S}_j = -\sqrt{-g}\nabla_i Q_{ij}$
- Compression
 - compute pressure
 - normalize velocity, update W
 - compute pressure again

- update energy, accounting for compressional heating:
 $\dot{E} = -P\nabla_i(WV^i)$
- Pressure gradient
 - compute pressure
 - update momentum, accounting for pressure gradients:
 $\dot{S}_j = -\sqrt{-g}\nabla_j P$
- Transport
 - compute pressure
 - normalize velocity, update W
 - update transport terms in all variables:
 $\dot{D} = -\nabla_i(DV^i)$, $\dot{E} = -\nabla_i(EV^i)$, and $\dot{S}_j = -\nabla_i(S_jV^i)$
- Boost factor
 - compute pressure and sound speed
 - normalize velocity, final update of W
 - update energy, accounting for the variation of W in time:
 $\dot{E} = -[P + (\sum_i Q_{ii}^2 / \sum_i Q_{ii})]\dot{W}$
- Update spacetime metric components $g_{\mu\nu}$ and $g^{\mu\nu}$ if time dependent

The highly nonlinear coupling of pressure and artificial viscosity to the state and kinematic variables through the Lorentz factor makes the relativistic equations much more difficult to solve than their Newtonian versions. It is for this reason that Norman & Winkler (1986) adopted implicit methods to solve the special relativistic equations. It is also why we have attempted to maintain a consistent and frequent update of the velocity normalization, boost factor, pressure and artificial viscosity throughout the cycle.

To enforce stable evolutions, the timestep is defined for all hydro methods as the minimum causality constraint over the entire mesh arising from the sound speed, fluid velocity, magnitude of the artificial viscosity coefficient, and any other physics criteria introduced in the calculation, say from scalar fields, radiation transport, gravity, etc... Also, since the timesteps can be nonuniform, a final constraint is added to prevent Δt from increasing by more than 20% per timestep. In short,

$$\Delta t^{n+1} = \min \left[\frac{k_c}{V_{max}}, 1.2 \times \Delta t^n \right], \quad (3-1)$$

where the superscript n refers to the discrete time level and the maximum velocity V_{max} (computed over all zones) accounts for local sound speed, fluid velocity, and viscous diffusion

$$V_{max} = \max \left[\frac{C_s}{\min(dx^i)}, \max \left(\frac{|V^i|}{dx^i} \right), 4k_{q2} \max(|V^i_{,i}|), 4k_{q2} \left| \sum_i V^i_{,i} \right| \right]. \quad (3-2)$$

The Courant factor k_c is typically set to $\lesssim 0.6$, the viscosity strength coefficient k_{q2} (defined in (3-8)) is set to 2.0 for all the problems presented in this paper, and the sound speed is defined as

$$C_s^2 = \frac{1}{h} \frac{\partial P}{\partial \rho} \Big|_s = \frac{\Gamma P}{\rho h} = \frac{\Gamma(\Gamma - 1)P}{(\Gamma - 1)(D/W) + \Gamma P}. \quad (3-3)$$

for relativistic flows, where we have explicitly used the adiabatic eos in the form $P \propto \rho^\Gamma$.

The artificial viscosity is implemented in a form that mimics a general nonperfect fluid stress tensor

$$T^{\mu\nu} = \rho h u^\mu u^\nu + P g^{\mu\nu} - 2\eta \sigma^{\mu\nu} - \xi \theta (g^{\mu\nu} + u^\mu u^\nu), \quad (3-4)$$

where η and ξ are the shear and bulk viscosity coefficients, $\theta = u^\mu_{;\mu}$ is the expansion of fluid world lines, and $\sigma^{\mu\nu}$ is the trace-free spatial shear tensor. Artificial viscosity is included as a bulk scalar viscosity so the effective perfect fluid stress energy tensor takes the form

$$T^{\mu\nu} = (\rho + e + P + Q) u^\mu u^\nu + (P + Q) g^{\mu\nu}, \quad (3-5)$$

which is equivalent to setting $P \rightarrow P + Q$ in the momentum and energy equations

$$\frac{\partial S_j}{\partial t} + \frac{\partial(S_j V^i)}{\partial x^i} - \frac{S^\mu S^\nu}{2S^0} \frac{\partial g_{\mu\nu}}{\partial x^j} + \sqrt{-g} \frac{\partial(P + Q_j)}{\partial x^j} = 0, \quad (3-6)$$

$$\frac{\partial E}{\partial t} + \frac{\partial(EV^i)}{\partial x^i} + \left(P + \frac{\sum_i Q_i^2}{\sum_i Q_i} \right) \frac{\partial W}{\partial t} + P \frac{\partial(WV^i)}{\partial x^i} + \sum_i Q_i \frac{\partial(WV^i)}{\partial x^i} = 0. \quad (3-7)$$

The scalar viscosity Q_i is computed as a local quantity in a dimensionally split fashion, and active only in convergent flows for which $\nabla_i V^i < 0$

$$Q_i = (D + E + PW) \Delta l (\nabla_i V^i) [k_{q2} \Delta l (\nabla_i V^i) (1 - \phi^2) - k_{q1} C_s]. \quad (3-8)$$

The coefficients k_{q2} and k_{q1} control the amount of quadratic and linear (in velocity) components of viscosity, Δl is a length scale set to the zone dimension, and ϕ represents a limiter bounded by zero and unity that can be applied to reduce the effect of artificial heating and narrow the width of shock fronts. One could alternatively use $W^{-1} \nabla_i (WV^i)$ in place of $\nabla_i V^i$

in (3-8), which we find to be effective at preventing excessively large jump errors and helps stabilize solutions in highly relativistic shock tube and wall shock calculations.

A more general tensor version of artificial viscosity is also implemented for convergent flows to the form (Tscharnutter & Winkler 1979)

$$Q_{ij} = (D + E + PW)\Delta l \left[k_{q2}\nabla_k V^k \Delta l - k_{q1}C_s \right] \left[\frac{1}{2}(\nabla_i V^j + \nabla_j V^i) - \frac{c}{3}\nabla_k V^k \delta_{ij} \right], \quad (3-9)$$

where c is a constant defined as zero or unity depending on whether the viscosity tensor should be traceless or not, and δ_{ij} is the Kronecker delta. The equations for energy and momentum with a tensor viscosity are similar to (3-6) and (3-7) except in the way two of the viscosity terms are computed

$$\begin{aligned} & \frac{\partial S_j}{\partial t} + \frac{\partial(S_j V^i)}{\partial x^i} - \frac{S^\mu S^\nu}{2S^0} \frac{\partial g_{\mu\nu}}{\partial x^j} + \sqrt{-g} \frac{\partial P}{\partial x^j} + \sqrt{-g} \frac{\partial Q_{jk}}{\partial x^k} \quad (3-10) \\ \frac{\partial E}{\partial t} + \frac{\partial(EV^i)}{\partial x^i} + \left(P + \frac{\sum_i Q_{ii}^2}{\sum_i Q_{ii}} \right) \frac{\partial W}{\partial t} + P \frac{\partial(WV^i)}{\partial x^i} + \frac{1}{2} \sum_{i,j} Q_{ij} \left(\frac{\partial(WV^i)}{\partial x^j} + \frac{\partial(WV^j)}{\partial x^i} \right) \quad (3-10) \end{aligned}$$

The scalar form of artificial viscosity (3-8) is used in all the tests presented in this paper.

The transport step is solved in a directionally split, flux conservative manner. For example, considering advection of the density field along the x -axis in a staggered mesh scheme, the solution to $\dot{D} = -\nabla_x(DV^x)$ is written

$$D_i^{n+1} = D_i^n - \frac{\Delta t^n}{\Delta x} \left[\tilde{D}_{i+1} V_{i+1} - \tilde{D}_i V_i \right], \quad (3-12)$$

where V_{i+1} is the face-centered velocity between zones i and $i + 1$, and \tilde{D}_i is a first order monotonic Taylor's approximation of D_i from the upwind cell center to the advection control volume center

$$\begin{aligned} \tilde{D}_i = & \left[\frac{1}{2} + \text{sign} \left(\frac{1}{2}, V_i \right) \right] \left[D_{i-1} + \frac{(\Delta x - V_i \Delta t)}{2} (\nabla_x D)_{i-1} \right] \\ & + \left[\frac{1}{2} - \text{sign} \left(\frac{1}{2}, V_i \right) \right] \left[D_i - \frac{(\Delta x + V_i \Delta t)}{2} (\nabla_x D)_i \right]. \quad (3-13) \end{aligned}$$

Equation (3-13) automatically detects the upwind cell from the sign of the velocity V . Here, $\text{sign}(1/2, V_i)$ is fortran notation for $\pm 1/2$, depending on the sign of V_i . High order van Leer (1977) monotonic interpolation is used to reconstruct local gradients $(\nabla_x D)_i$ and prevent spurious oscillations near regions of sharp gradients

$$(\nabla_x D)_i = \left[\frac{1}{2} + \text{sign} \left(\frac{1}{2}, \Delta D_i \Delta D_{i-1} \right) \right] \left(\frac{2\Delta D_i \Delta D_{i-1}}{\Delta D_i + \Delta D_{i-1} + \delta} \right). \quad (3-14)$$

The constant $\delta \ll 1$ is introduced to prevent numerical overflow, and $\Delta D_i = (D_{i+1} - D_i)/\Delta x$ are the mesh aligned gradients centered on the cell faces. Similar expressions can easily be derived for zone-centered variables on nonstaggered meshes by face-averaging the velocities, and for face-centered variables on staggered meshes by shifting the spatial indices and control volumes appropriately.

3.2. Non-oscillatory Central Difference Schemes

Considering the simplicity of equations (2-11) - (2-13), an obvious benefit of the NOCD approach is that, unlike the AV approach, it is not expected to be particularly sensitive to any ordering of operator updates since the method basically just solves a single first order operator equation with external sources. We have implemented two variations of this method: the first with non-staggered spatial and temporal meshes with second order reconstruction, and the second with time-staggered meshes in which the variables are updated on a mesh shifted in time to center the solution properly to second order. A summary of the solver sequence for this class of methods is:

- Compute timestep Δt from (3-1),
 redefine $\Delta t \rightarrow \Delta t/2$ for the 2-step, subcycled, staggered mesh scheme
- Curvature
 - compute pressure from the ideal fluid equation of state:

$$P = (\Gamma - 1)[\mathcal{E}\sqrt{-g}/(W^2) - D/W]/[\Gamma + (\Gamma - 1)g^{00}(\sqrt{-g}/W)^2]$$
 - update energy and momentum, accounting for curvature:

$$\dot{\mathcal{E}} = \Sigma^0 \text{ and } \dot{\mathcal{S}}^j = \Sigma^j, \text{ using second order finite differencing for metric derivatives}$$
- Flux operator
 - compute pressure from eos
 - normalize velocity and update boost factor:

$$V^i = S^i/S^0, \text{ using } S_\mu S^\mu = -M^2 = -[(\mathcal{E} - \sqrt{-g}g^{00}P)\sqrt{-g}/W]^2 \text{ and}$$

$$S^i = \mathcal{S}^i - \sqrt{-g}g^{0i}P \text{ to first compute } S^0, \text{ then the boost factor } W = \sqrt{-g}S^0/M$$
 - compute pressure
 - update all variables $\omega \equiv (D, E, \mathcal{S}^j)$,
 accounting for flux-conservative gradient terms in equations (2-11) - (2-13):

$$\dot{\omega} = -\nabla_i[\omega V^i + \sqrt{-g}P(g^{i\alpha} - g^{0\alpha}V^i)]$$

- if the mesh is nonstaggered in time:
perform interpolations to recenter variables on the original unstaggered mesh

$$\omega_j^{n+1} = (\omega_{j-1/2}^{n+1} + \omega_{j+1/2}^{n+1})/2 + (\omega_{j-1/2}^{n+1'} - \omega_{j+1/2}^{n+1'})/8$$
- If the mesh is staggered:
 - repeat curvature and flux steps to evolve solution from $t = t^{n+1/2}$ to t^{n+1}
 - shift array indices to realign final coordinates at t^{n+1} with
initial coordinates at t^n by $\omega_{i,j,k} = \omega_{i-1,j-1,k-1}$
- Update spacetime metric components $g_{\mu\nu}$ and $g^{\mu\nu}$ if time dependent

Two essential assumptions built into this method are that the cell-averaged solutions can be reconstructed as MUSCL-type piece-wise linear interpolants, and that the flux integrals are defined and evaluated naturally on staggered meshes. Since we adopt directional splitting for multi-dimensional problems, the basic discretization scheme used to solve equations (2-11) - (2-13) can be derived from a simple one-dimensional, first order model equation of the form

$$\frac{\partial \omega}{\partial t} + \frac{\partial f(\omega)}{\partial x} = 0, \quad (3-15)$$

where ω represents any of the density, energy or momentum variables, and $f(\omega)$ is the associated flux. A formal solution to (3-15) can be written over a single time cycle ($t^n \rightarrow t^{n+1}$) on a staggered mesh as

$$\omega_{j+1/2}(t^{n+1}) = \omega_{j+1/2}(t^n) - \frac{\Delta t}{\Delta x} \left[\frac{1}{\Delta t} \int_{t^n}^{t^{n+1}} f(\omega_{j+1}(\tau)) d\tau - \frac{1}{\Delta t} \int_{t^n}^{t^{n+1}} f(\omega_j(\tau)) d\tau \right]. \quad (3-16)$$

Introducing the notation $\omega'_j = \omega_{j+1} - \omega_{j-1}$, the average of the piece-wise linearly reconstructed solutions at the staggered positions $\omega_{j+1/2}(t^n)$ in (3-16) is given by

$$\omega_{j+1/2} = \frac{1}{2}(\omega_{j+1/2}^+ + \omega_{j+1/2}^-) = \frac{1}{2}(\omega_j + \omega_{j+1}) + \frac{1}{8}(\omega'_j - \omega'_{j+1}), \quad (3-17)$$

where $\omega_{j+1/2}^\pm$ refer to the piecewise linearly interpolated solutions from the upwind and downwind cell centers

$$\omega_{j+1/2}^+ = \omega_{j+1} - \frac{1}{4}(\omega_{j+2} - \omega_j), \quad (3-18)$$

$$\omega_{j+1/2}^- = \omega_j + \frac{1}{4}(\omega_{j+1} - \omega_{j-1}). \quad (3-19)$$

Considering that the time averaged integrals in (3-16) can be approximated using mid-point values

$$\frac{1}{\Delta t} \int_{t^n}^{t^{n+1}} f(\omega_j(\tau)) d\tau \sim f(\omega_j(t^{n+1/2})), \quad (3-20)$$

immediately suggests a two step predictor-corrector procedure to solve (3-15): the state variables are predicted at $t = t^{n+1/2}$ by

$$\omega_j^{n+1/2} = \omega_j^n - \frac{\Delta t}{2\Delta x} f'(\omega_j), \quad (3-21)$$

then corrected on the staggered mesh by

$$\omega_{j+1/2}^{n+1} = \frac{1}{2}(\omega_j^n + \omega_{j+1}^n) + \frac{1}{8}(\omega'_j - \omega'_{j+1}) - \frac{\Delta t}{\Delta x} \left[f(\omega_{j+1}^{n+1/2}) - f(\omega_j^{n+1/2}) \right], \quad (3-22)$$

where we have also substituted (3-17) for $\omega_{j+1/2}(t^n)$ in (3-16). Equations (3-21) and (3-22) represent the complete single cycle solution averaged on a staggered mesh. The mesh indices can be brought back into alignment by setting $\Delta t \rightarrow \Delta t/2$, performing two time cycle updates (computing $\omega_{j+1/2}^{n+1/2}$ then ω_{j+1}^{n+1}) to time $t^{n+1} = t^n + \Delta t$, and re-center the solution on the original zone positions by shifting the array indices as $\omega_j = \omega_{j-1}$.

As an alternative to mesh staggering, the solution after applying the corrector step can be reconstructed directly back to the nonstaggered cell centers by a second order piece-wise linear extrapolation

$$\omega_j^{n+1} = \frac{1}{2}(\omega_{j-1/2}^{n+1} + \omega_{j+1/2}^{n+1}) + \frac{1}{8}(\omega_{j-1/2}^{n+1'} - \omega_{j+1/2}^{n+1'}), \quad (3-23)$$

to yield for the final single timestep solution

$$\begin{aligned} \omega_j^{n+1} = & \frac{1}{4}(\omega_{j-1}^n + 2\omega_j^n + \omega_{j+1}^n) - \frac{1}{16}(\omega_{j+1}^{n'} - \omega_{j-1}^{n'}) \\ & - \frac{\Delta t}{2\Delta x} \left[f(\omega_{j+1}^{n+1/2}) - f(\omega_{j-1}^{n+1/2}) \right] - \frac{1}{8}(\omega_{j+1/2}^{n+1'} - \omega_{j-1/2}^{n+1'}). \end{aligned} \quad (3-24)$$

We have found no substantial differences between the staggered and unstaggered approaches in all the test calculations we have performed. Hence all subsequent results presented in this paper from this class of algorithms are derived with the nonstaggered mesh method using (3-21) and (3-24).

One final important element of this method is that all gradients (of either the state variables ω'_j or fluxes $f'(\omega_j)$) must be processed and limited for monotonicity in order to guarantee non-oscillatory behavior. This is accomplished with either the minmod limiter

$$\omega'_j = \max \left(0, \min \left(1, \frac{\omega_j - \omega_{j-1}}{\omega_{j+1} - \omega_j} \right) \right) (\omega_{j+1} - \omega_j), \quad (3-25)$$

or the van Leer limiter

$$\omega'_j = \left[\frac{|(\omega_j - \omega_{j-1})/(\omega_{j+1} - \omega_j)| + (\omega_j - \omega_{j-1})/(\omega_{j+1} - \omega_j)}{1 + |(\omega_j - \omega_{j-1})/(\omega_{j+1} - \omega_j)|} \right] (\omega_{j+1} - \omega_j), \quad (3-26)$$

which satisfy the TVD constraints with appropriate Courant restrictions, although we note that steeper limiters can yield undesirable results especially in under-resolved high boost shock tube calculations.

4. Code Tests

4.1. Relativistic Shock Tube

We begin testing the staggered AV and nonstaggered NOCD methods with one of the standard problems in fluid dynamics, the shock tube. This test is characterized initially by two different fluid states separated by a membrane. At $t = 0$ the membrane is removed and the fluid evolves in such a way that five distinct regions appear in the flow: an undisturbed region at each end, separated by a rarefaction wave, a contact discontinuity, and a shock wave. This problem only checks the hydrodynamical elements of the code, as it assumes a flat background metric. However, it provides a good test of the shock-capturing properties of the different methods since it has an exact solution (Thompson 1986) against which the numerical results can be compared.

Two cases of the shock tube problem are considered first: moderate boost ($W = 1.43$) and high boost ($W = 3.59$) shock waves. In the moderate boost case, the initial state is specified by $\rho_L = 10$, $P_L = 13.3$, and $V_L = 0$ to the left of the membrane and $\rho_R = 1$, $P_R = 10^{-6}$, and $V_R = 0$ to the right. In the high boost case, $\rho_L = 1$, $P_L = 10^3$, $V_L = 0$, and $\rho_R = 1$, $P_R = 10^{-2}$, $V_R = 0$. In both cases, the fluid is assumed to be an ideal gas with $\Gamma = 5/3$, and the integration domain extends over a unit grid from $x = 0$ to $x = 1$, with the membrane located at $x = 0.5$. Most of the AV shock tube results presented here were run using the scalar artificial viscosity with a quadratic viscosity coefficient $k_{q2} = 2.0$, linear viscosity coefficient $k_{q1} = 0.3$, and Courant factor $k_c = 0.6$. A couple of the highest boost runs presented in Table 3 are the only exceptions. In these cases the viscosity coefficients were kept the same but the Courant factor was varied as needed to maintain stability. We have carried out these tests in one, two and three dimensions, lining up the interface membrane along the main diagonals in multi-dimensional runs. For the NOCD method we use $k_c = 0.3$ and the minmod limiter which gives smoother and more robust results than the steeper limiters in simulations of under-resolved highly relativistic shocks.

Figures 1 & 2 show spatial profiles of the moderate boost results at time $t = 0.4$ on a

grid of 400 uniformly spaced zones using the AV and NOCD methods respectively. Figures 3 & 4 show the corresponding solutions of both AV and NOCD methods for the high boost test using a higher resolution grid with 800 zones at time $t = 0.36$. Tables 1 & 2 summarize the errors in the primitive variables ρ , P , and V for different grid resolutions and CFD methods using the L_1 norm (i.e., $\|E(a)\|_1 = \sum_{i,j,k} \Delta x_i \Delta y_j \Delta z_k |a_{i,j,k}^n - A_{i,j,k}^n|$, where $a_{i,j,k}^n$ and $A_{i,j,k}^n$ are the numerical and exact solutions, respectively, and for 1D problems the orthogonal grid spacings are set to unity). Included in Table 1 for comparison are the errors reported by Font et al. (2000) using Marquina’s approximate Riemann solver (Donat & Marquina 1996). They also tested the Roe and Flux-split approximate solvers and achieved similar results as with Marquina’s method, so we do not include those numbers here. We find the errors in Table 1 are quite comparable between all three methods with convergence rates just under first order as expected for shock capturing methods. For the high boost case in Table 2, our errors are comparable to those reported by Martí & Müller (1996) for the same shock tube simulation using an extended high order piecewise parabolic method (PPM) (Colella & Woodward 1984) with an exact Riemann solver. However, we note that their published errors are for the conserved quantities (generalized fluid density D , generalized energy density $\tau = \rho h W^2 - P - D$, and covariant momentum density S) rather than the primitive variables we report. Their results are included in Table 2. We also note that the slightly larger errors in the 3D AV results of Table 1 are due primarily to boundary effects (particularly at the grid corners) and not to shock capturing differences. In fact, errors computed only along the main diagonal are about the same for the NOCD and AV methods.

Table 3 shows the mean-relative errors (defined as $\bar{\epsilon}_{\text{rel}}(a) = \sum_{i,j,k} |a_{i,j,k}^n - A_{i,j,k}^n| / \sum_{i,j,k} |A_{i,j,k}^n|$, where again $a_{i,j,k}^n$ and $A_{i,j,k}^n$ are the numerical and exact solutions, respectively) in the primitive variables over a range of boost factors using 800 zones to cover the same unit domain. The different boost factors are established by systematically increasing the original value of P_L over the moderate boost case. These errors are also displayed graphically in Figure 5, comparing the AV and NOCD methods up to about the maximum boost for which the AV approach can be pushed reliably at these grid resolutions. The increasing trend (with boost) in error reflects the stronger nonlinear coupling through the fluid velocity and the narrower and steeper leading shock plateau as evidenced in the density plots. At 800 zone resolution, the leading density plateau for the high boost case is covered by fewer than nine cells in the analytic solution, compared to about thirty-six zones for the corresponding moderate boost calculation. For shock velocities greater than about $V \sim 0.95$, the AV results become increasingly unstable and uncertain with respect to parameter choices (resolution, Courant factor, viscosity strengths, etc...). However, over the range in which AV results are robust, the errors are comparable between the AV, NOCD, and Godunov methods.

4.2. Relativistic Wall Shock

A second test presented here is the wall shock problem involving the shock heating of cold fluid hitting a wall at the left boundary ($x = 0$) of a unit grid domain. The initial data are set up to be uniform across the grid with adiabatic index $\Gamma = 4/3$, pre-shocked density $\rho_1 = 1$, pre-shocked pressure $P_1 = 7.63 \times 10^{-6}$, and velocity $V_1 = -v_{init} = -(1 - \nu)$, where $\nu < 1$ is the infall velocity parameter. When the fluid hits the wall a shock forms and travels to the right, separating the pre-shocked state composed of the initial data and the post-shocked state with solution in the wall frame

$$V_S = \frac{\rho_1 W_1 V_1}{\rho_2 - \rho_1 W_1}, \quad (4-1)$$

$$P_2 = \rho_2 (\Gamma - 1) (W_1 - 1), \quad (4-2)$$

$$\rho_2 = \rho_1 \left[\frac{\Gamma + 1}{\Gamma - 1} + \frac{\Gamma}{\Gamma - 1} (W_1 - 1) \right], \quad (4-3)$$

where V_S is the velocity of the shock front, and the pre-shocked energy and post-shocked velocity were both assumed negligible ($\epsilon_1 = V_2 = 0$). To facilitate a direct comparison between our results and the Genesis code of Aloy, Ibáñez, & Martí (1999) (which again uses Marquina’s approximate Riemann solver) all of the results shown in the figures and tables, unless noted otherwise, were performed on a 200 zone uniformly spaced mesh and ran to a final time of $t = 2.0$. Also, for the NOCD methods, the courant factor is set to $k_c = 0.3$, and we use the van Leer limiter for gradient calculations, which generally gives smaller errors when compared to the more diffusive minmod limiter (about a 30% reduction for the lower boost cases we have tried). For the AV methods, we use the scalar viscosity with $k_c = 0.6$, $k_{q1} = 0.3$, and $k_{q2} = 2.0$ for all the runs.

Figures 6 & 7 show spatial profiles for the case with initial velocity $v_{init} = 0.9$ and 200 zones for the AV and NOCD methods, respectively. Table 4 summarizes the $L-1$ norm errors in both methods as a function of grid resolution. The values given in parentheses are the contributions to the total error in the first twenty zones from the reflection wall at $x = 0$. These numbers clearly indicate a disproportionate error distribution from wall heating, an effect that is especially evident in the AV results. Excluding this contribution may give a more accurate assessment of each method’s ability to resolve the actual shock profile.

Figure 8 plots the mean-relative errors (using 200 zones) in density, which are generally greater than errors in either the pressure or velocity, as a function of boost factor up to about the maximum boost that the AV methods can be run accurately. Although we are not able to extend the AV method reliably beyond $v_{init} \sim 0.97$, the NOCD methods, on the other hand, are substantially more robust. In fact, as shown in Table 5 and Figure 9, the NOCD schemes can be run up to arbitrarily high boost factors with stable mean relative

errors, typically less than two percent with no significant increasing trend. These errors are generally smaller than those quoted by Aloy, Ibáñez, & Martí (1999). We note that the errors for the AV method presented in Figure 8 and Table 5 can be improved significantly by either lowering the Courant factor or increasing the viscosity coefficients. For example, decreasing k_c from 0.6 to 0.3, or increasing k_{q2} from 2 to 3 for the case $v_{init} = 0.95$ reduces the $L-1$ norm in density from 0.116 to 0.048 and 0.033, respectively. We have also been able to run wall shock tests with the AV method at slightly higher boosts than shown in Table 5 by choosing different parameter combinations (e.g., $k_c = 0.2$, $k_{q1} = 1.0$ and 400 zones can evolve flows with $v_{init} = 0.99$ fairly accurately). However, rather than adjusting parameters to achieve the best possible result for each specific problem, we have opted to keep numerical parameters constant between code tests, boost factors, and numerical methods.

4.3. Black Hole Accretion

As a test of hydrodynamic flows in spacetimes with nontrivial curvature, we consider radial accretion of an ideal fluid onto a compact, strongly gravitating object, in this case a Schwarzschild black hole. The fluid will accrete onto the compact object along geodesics, thus allowing the general relativistic components of our codes to be tested against a well-known analytic stationary solution. Assuming a perfect fluid in isotropic Schwarzschild coordinates

$$ds^2 = - \left(\frac{1 - M/2\rho}{1 + M/2\rho} \right)^2 dt^2 + \left(1 + \frac{M}{2\rho} \right)^4 (dx^2 + dy^2 + dz^2), \quad (4-4)$$

where $\rho = \sqrt{x^2 + y^2 + z^2}$ is the isotropic radius, the exact solution to this problem is dependent on a single parameter, the gravitational binding energy (u_0). In terms of this parameter (which we set to $u_0 = -1$ in our tests), the solution can be written

$$W = \sqrt{-g} g^{00} u_0, \quad (4-5)$$

$$D = \frac{C_D}{\rho^2 V^\rho}, \quad (4-6)$$

$$E = \frac{C_E}{W^{\Gamma-1} (\rho^2 V^\rho)^\Gamma}, \quad (4-7)$$

$$V^\rho = -\frac{u^\rho}{u^0} = -\frac{1}{g^{00} u_0} \sqrt{-g^{\rho\rho} (1 + g^{00} u_0^2)}, \quad (4-8)$$

where W is the boost factor, V^ρ is the radial infall velocity in isotropic radial coordinates, D is the generalized density in isotropic Cartesian coordinates, E is the generalized internal energy in isotropic Cartesian coordinates, $\Gamma = 5/3$ is the adiabatic index, and C_D and C_E are constants of integration which we set to $C_D = 1$ and $C_E = C_D/100$ in the simulations.

The computational domain for this problem is constructed to be $(5M)^3$ (where $M = 1$ is the black hole mass) and centered along the z -axis with $-2.5M \leq (x, y) \leq 2.5M$. In the z -direction the inner boundary zone $z = z_{min}$ is defined to lie outside the event horizon at $z_{min} = 1.5M$ in isotropic coordinates to guarantee all boundary zones are outside the horizon, and extends to $z = z_{max} = 6.5M$ along the $x = y = 0$ line. Calculations are carried out on different resolution grids, ranging from 16^3 to 64^3 to check code convergence. All variables are initially set to negligible values throughout the interior domain ($D = 10^{-2}$, $E = DC_E/C_D$, $W = 1$, and $S_i = V^i = 0$), and the static analytic solutions are specified as outer boundary conditions at all times. Along the inner z boundary, outflow conditions are maintained by simply setting the first derivatives of all variables to zero at the end of each timestep. Thus fluid flows onto the computational grid from all of the analytically-specified (inflow) boundaries, and exits from the lower z -plane closest to the black hole. All results presented here were generated from simulations run until steady-state was achieved at $t = 50M$, and numerical parameters are defined as in previous tests, namely $k_c = 0.6$, $k_{q1} = 0$, $k_{q2} = 2.0$ in the AV runs, and $k_c = 0.3$ in the NOCD results. Table 6 summarizes the global mean-relative errors in both methods as a function of grid resolution. Figures 10 & 11 show spatial profiles of density and velocity along the z -axis for 32^3 and 64^3 zones for the AV and NOCD methods, respectively.

Although the numerical results in Table 6 converge to the analytic solution with grid resolution, they converge at a rate between first and second order due in part to the treatment of boundary conditions and time discretization errors. In particular, comparing the analytic and numerical solutions, we find that maximum relative errors occur near the event horizon along the inner z -boundary. For the AV method, the maximum relative errors for density and velocity with 64^3 zones are 9.16% and 2.49%, respectively, compared to global mean-relative errors of 1.36% and 0.63%. For the NOCD method, the maximum relative errors are 24.4% and 7.42%, compared to global mean-relative errors of 2.11% and 0.14%. The global errors in both methods, in spite of being computed on a nonsymmetric Cartesian mesh, are comparable to those reported by other authors. For instance, Hawley, Smarr, & Wilson (1984b) saw relative errors of 1-3% in density and velocity near the horizon using an artificial viscosity code on a 25×10 cylindrical grid. Banyuls et al. (1997) saw mean relative errors of 2.67% and 0.99% using a Godunov-type method on a 200×5 spherical grid. Also, decreasing the Courant factor from $k_c = 0.6$ to 0.2 reduces the errors in both AV and NOCD methods by about a factor of three, consistent with first order time discretization, and increases the rate of spatial convergence closer to second order.

5. Conclusion

We have developed new artificial viscosity and non-oscillatory central difference numerical hydrodynamics schemes as integral components of the Cosmos code framework for performing fully general relativistic calculations of strong field flows. These methods have been discussed at length here and compared also with published state-of-the-art Godunov methods on their abilities to model shock tube, wall shock and black hole accretion problems. We find that for shock tube problems at moderate to high boost factors, with velocities up to $V \sim 0.95 - 0.99$, the artificial viscosity methods compare quite favorably with the NOCD methods, the Godunov methods using the Marquina, Roe, or Flux-split approximate Riemann solvers, and the piecewise parabolic method with an exact Riemann solver. However, they tend to become unstable or at least highly sensitive to parameters and generally unreliable at higher boosts ($V \gtrsim 0.95$). On the other hand, NOCD methods can easily be extended to ultra-relativistic velocities ($1 - V < 10^{-11}$) as demonstrated by the wall shock tests carried out in this paper, and are comparable in accuracy over the entire range of velocities we have simulated to the more standard but complicated Riemann solver codes. NOCD schemes thus provide a robust new alternative to simulating relativistic hydrodynamical flows since they offer the same advantages of Godunov methods in capturing ultra-relativistic flows but without the cost and complication of Riemann solvers or flux splitting. They also provide all the advantages of AV methods in their speed, ease of implementation, and general applicability without explicitly using artificial viscosity for shock capturing.

This work was performed under the auspices of the U.S. Department of Energy by University of California, Lawrence Livermore National Laboratory under Contract W-7405-Eng-48.

REFERENCES

- Aloy, M. A., Ibáñez, J. M., and Martí, J. M. 1999, *ApJS*, 122, 151
- Anninos, P. 1998, *Phys. Rev. D*, 58, 064010
- Banyuls, F., Font, J. A., Ibáñez, J. M., Martí, J. M. and Miralles, J. A. 1997, *ApJ*, 476, 221
- Centrella, J. and Wilson, J. R. 1984, *ApJS*, 54, 229
- Colella, P. and Woodward, P. R. 1984, *J. Comput. Phys.*, 54, 174
- Donat, R. and Marquina, A. 1996, *J. Comput. Phys.*, 125, 42
- Eulderink, F. and Mellema, G. 1995, *Astron. Astrophys. Suppl. Ser.*, 110, 587
- Font, J. A., Miller, M., Suen, W. and Tobias, M. 2000, *Phys. Rev. D*, 61, 044011
- Hawley, J. F., Smarr, L. L. and Wilson, J. R. 1984, *ApJ*, 277, 296
- Hawley, J. F., Smarr, L. L. and Wilson, J. R. 1984, *ApJS*, 55, 211
- Jiang, O.-S., Levy, D., Lin, C.-T., Osher, S. and Tadmor, E. 1998, *SIAM J. Numer. Anal.*, 35, 2147
- Jiang, O.-S. and Tadmor, E. 1998, *SIAM J. Sci. Comput.*, 19, 1892
- Martí, J. and Müller, E. 1996, *J. Comput. Phys.*, 123, 1
- May, M. M. and White, R. H. 1966, *Phys. Rev. D*, 141, 1232
- May, M. M. and White, R. H. 1967, *Meth. Computat. Phys.*, 7, 219
- Norman, M. L. and Winkler, K.-H. A. 1986, in *Astrophysical Radiation Hydrodynamics*, ed. M. L. Norman & K.-H. A. Winkler (NATO ASI ser. C, 188) (Dordrecht:Reidel), 449
- Quirk, J. J., 1994, *Int. J. for Numerical Methods in Fluids*, 18, 555
- Thompson, K. W. 1986, *J. Fluid Mech.*, 171, 365
- Tscharnutter, W.-M. and Winkler, K.-H. 1979, *Comput. Phys. Comm.*, 18, 171
- van Leer, B. 1977, *J. Comput. Phys.*, 23, 276
- VonNeumann, J. and Richtmyer, R. D. 1950, *J. Appl. Phys.*, 21, 232
- Wilson, J. R. 1972, *ApJ*, 173, 431

Wilson, J. R., in *Sources of Gravitational Radiation*, edited by L. Smarr (Cambridge University Press, Cambridge, England, 1979)

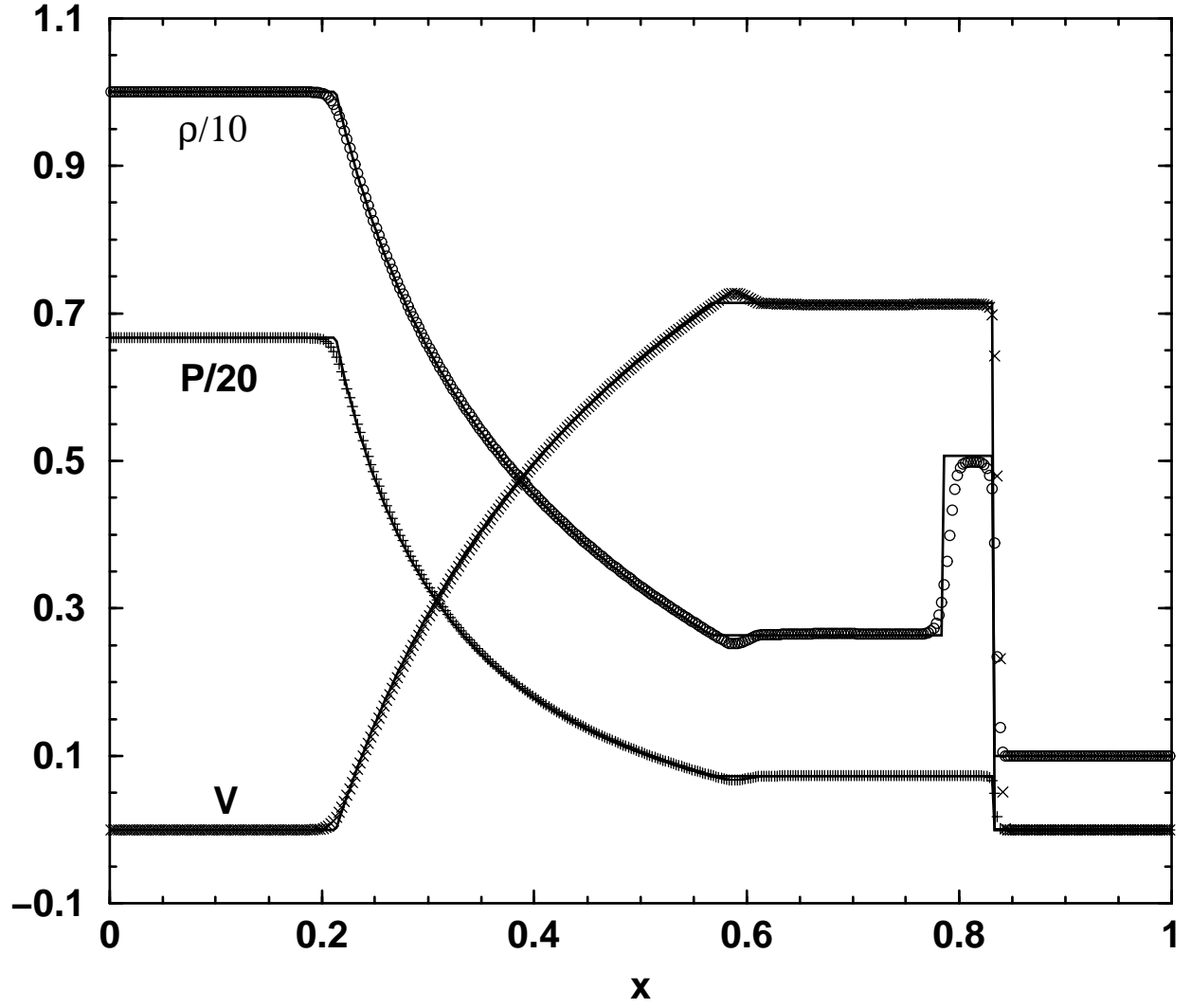


Fig. 1.— Normalized results for the moderate boost shock tube test using artificial viscosity for shock capturing and 400 zones to cover a unit grid. The solution is shown at time $t = 0.4$.

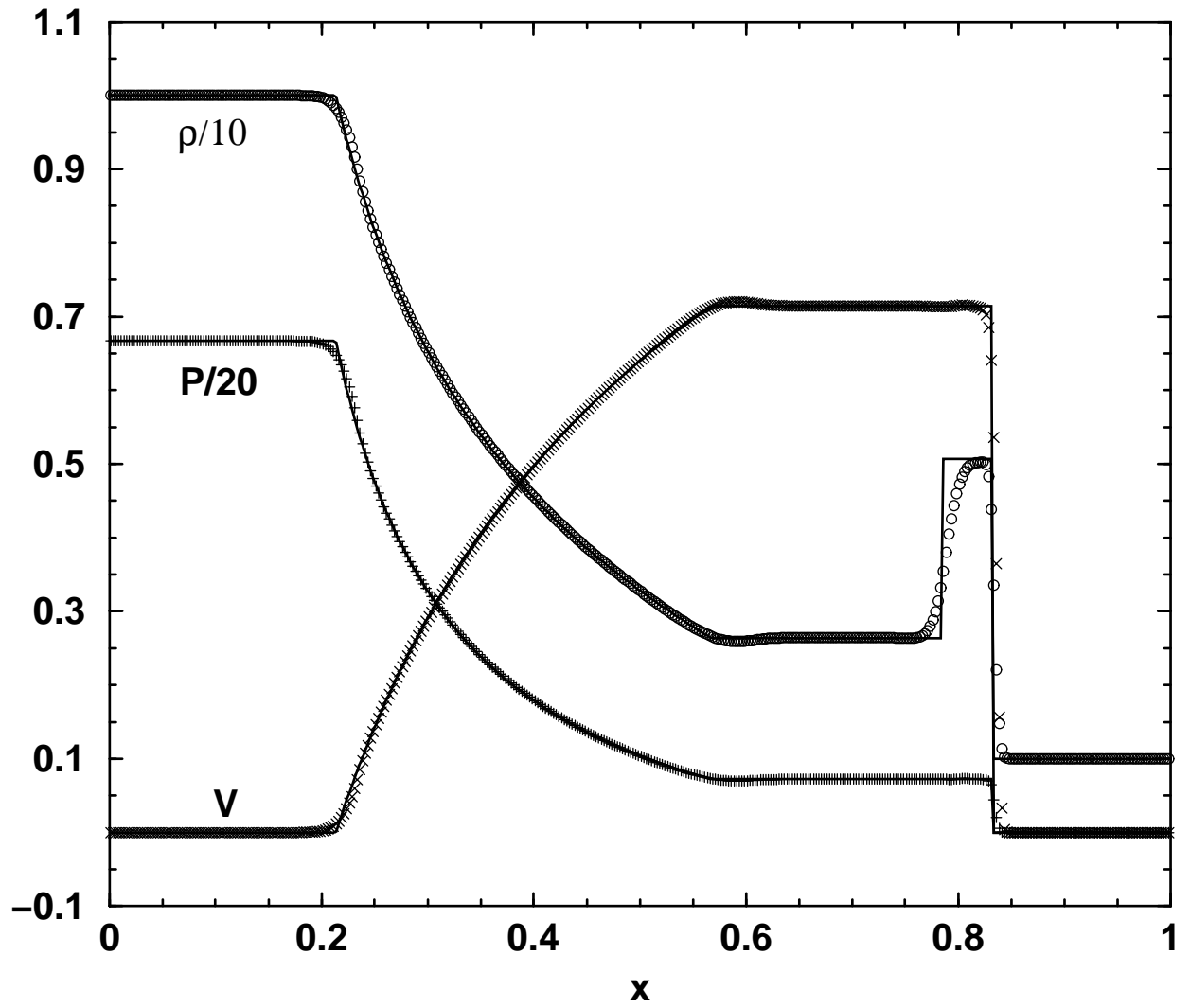


Fig. 2.— As Figure 1 except the solutions are computed using the non-oscillatory central difference scheme.

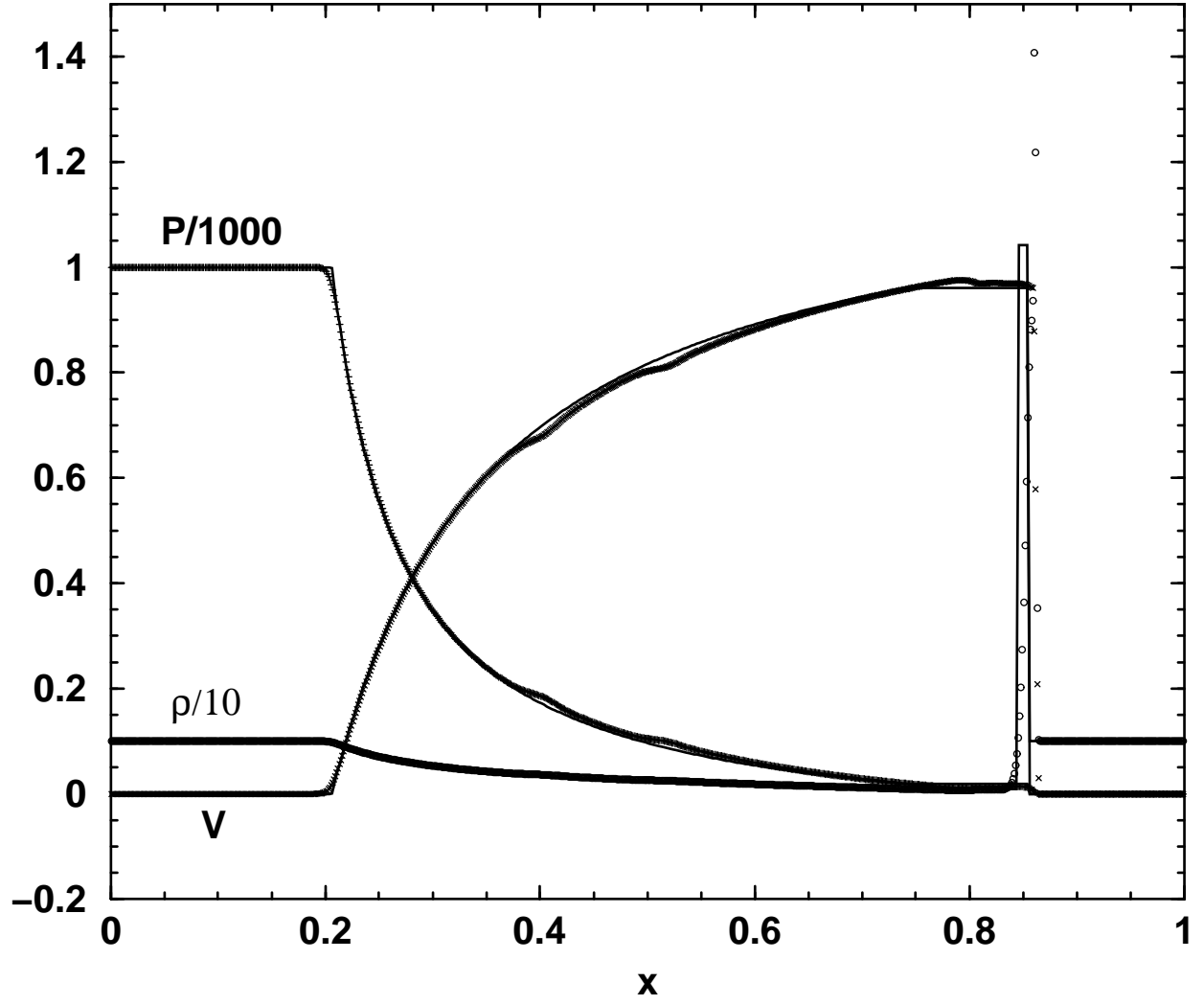


Fig. 3.— Results at time $t = 0.36$ for the high boost shock tube test using artificial viscosity and 800 zones.

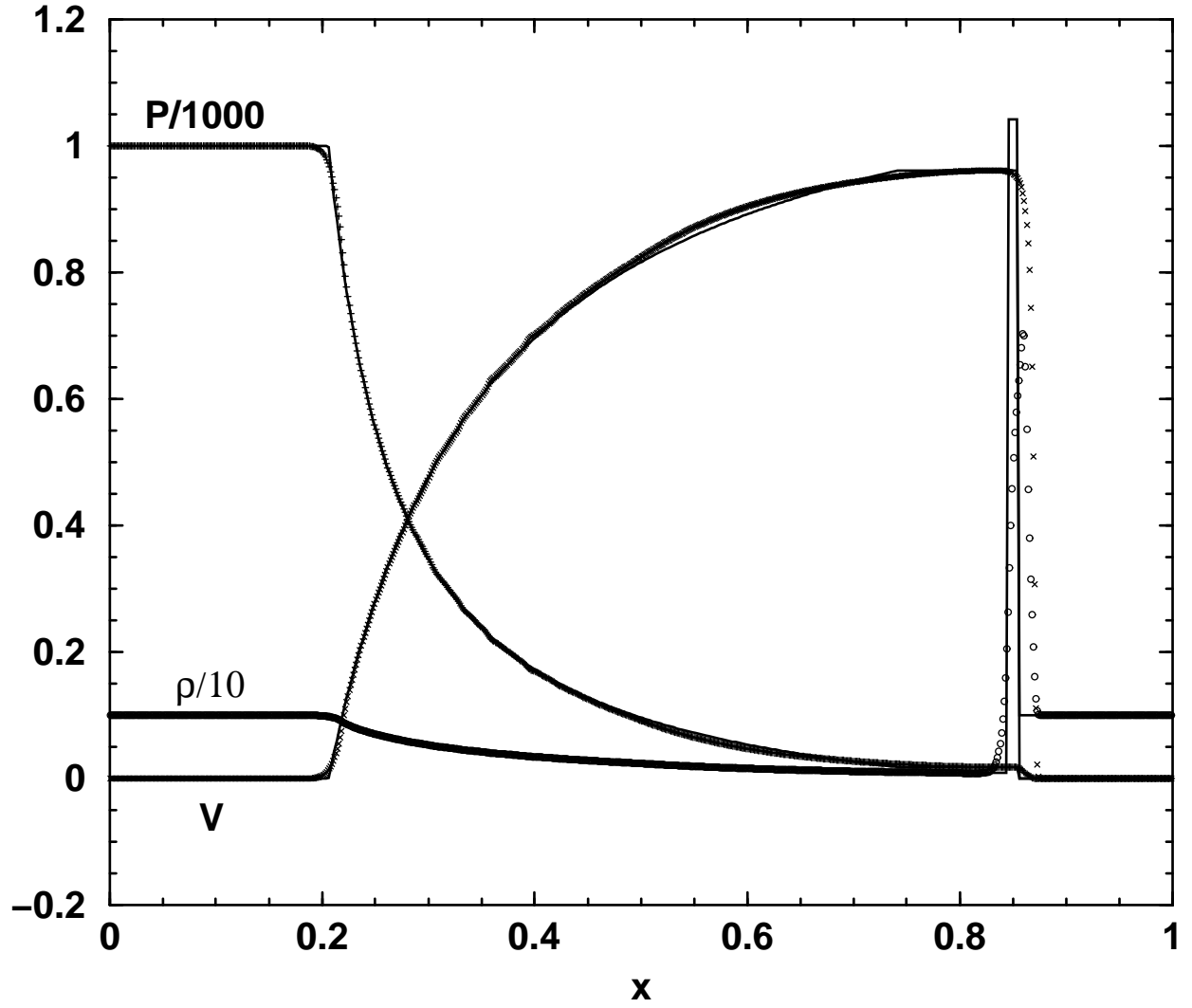


Fig. 4.— As Figure 3 but with the non-oscillatory central difference scheme.

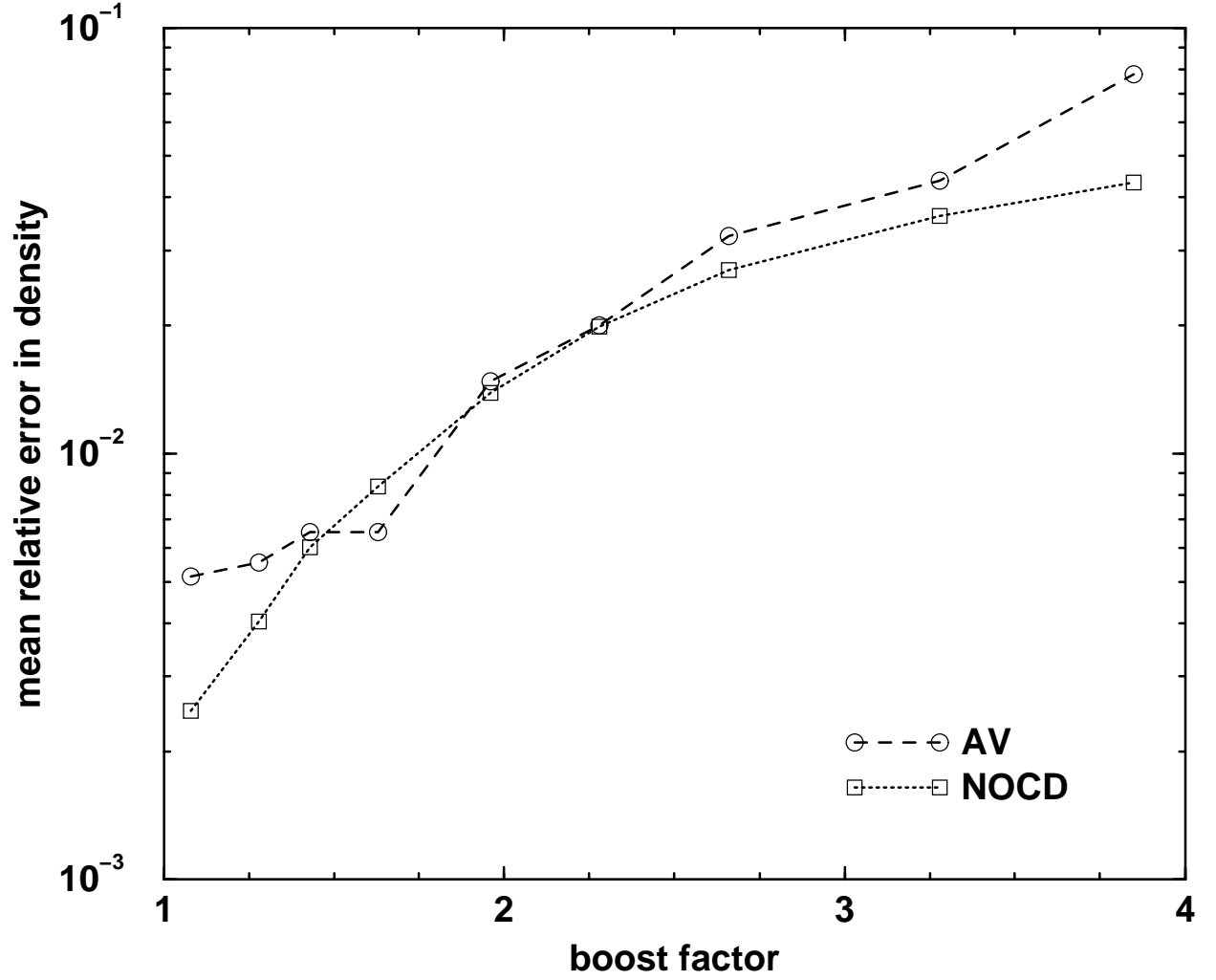


Fig. 5.— Mean relative errors in density for both the AV and NOCD methods as a function of boost for the relativistic shock tube problem. All calculations were run using 800 zones up to time $t = 0.36$.

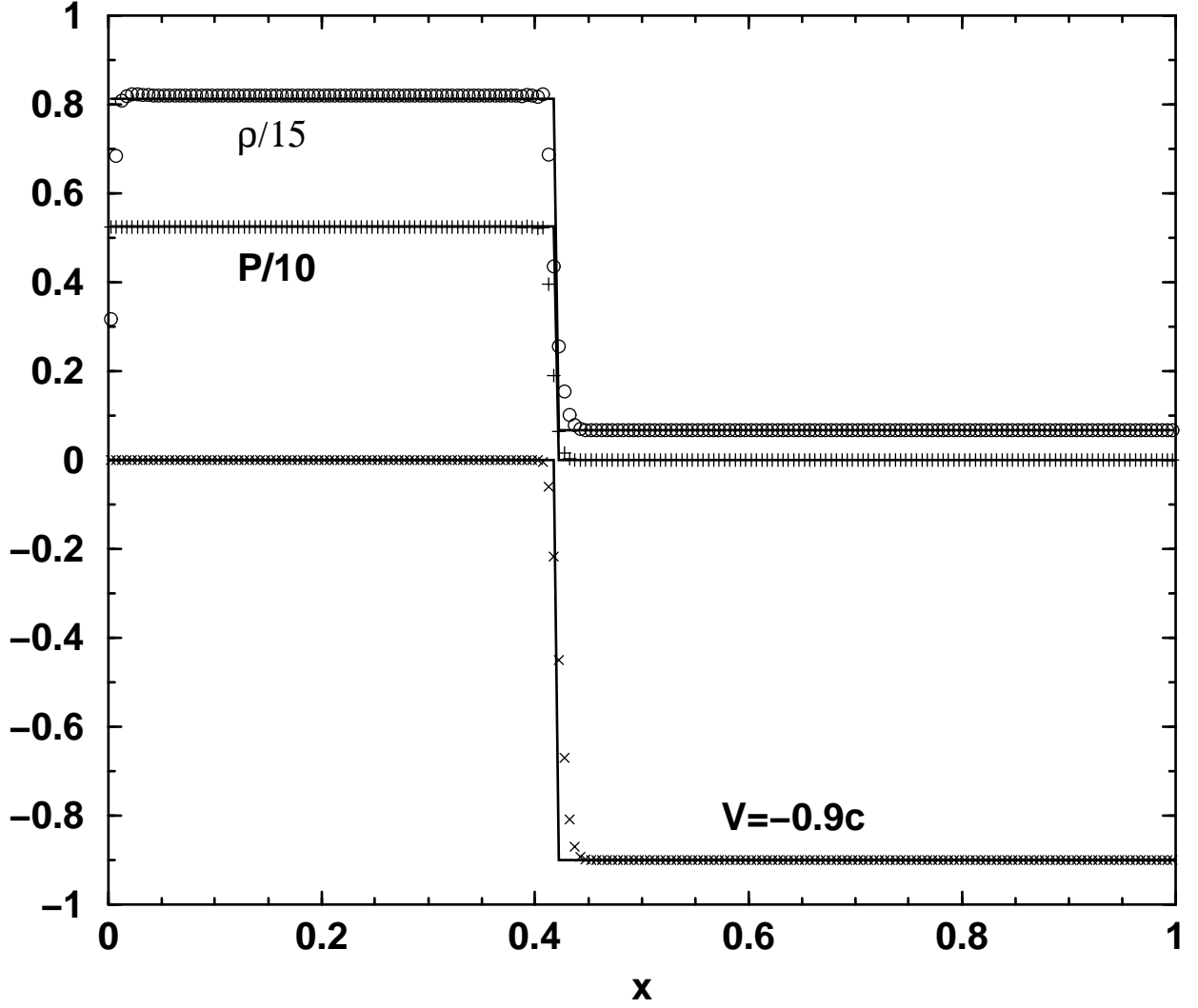


Fig. 6.— Results for the relativistic wall shock test with 200-zone resolution and infall velocity $V = -0.9c$ using artificial viscosity. The solution is shown at time $t = 2.0$.

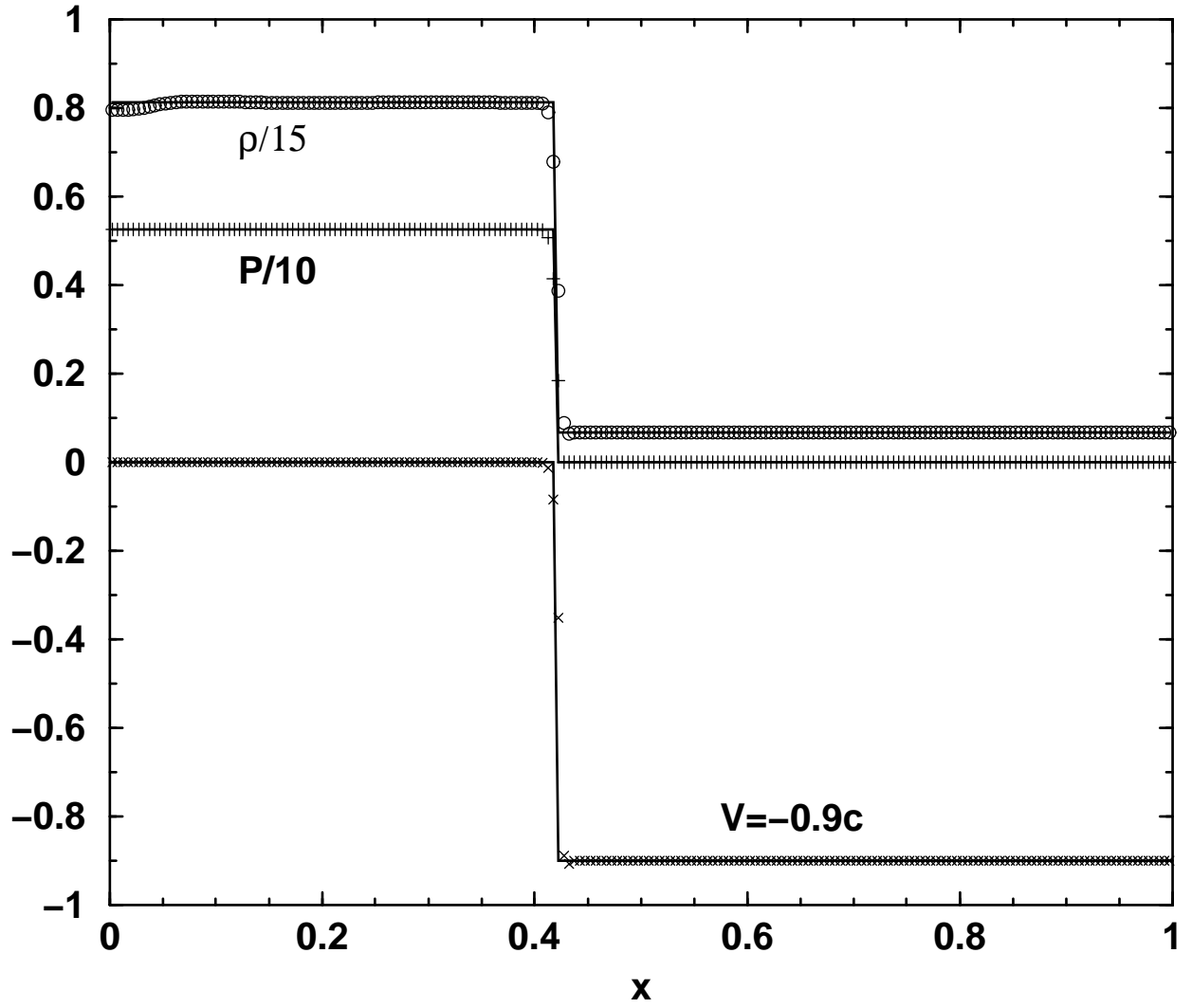


Fig. 7.— As Figure 6 but for the NOCD scheme.

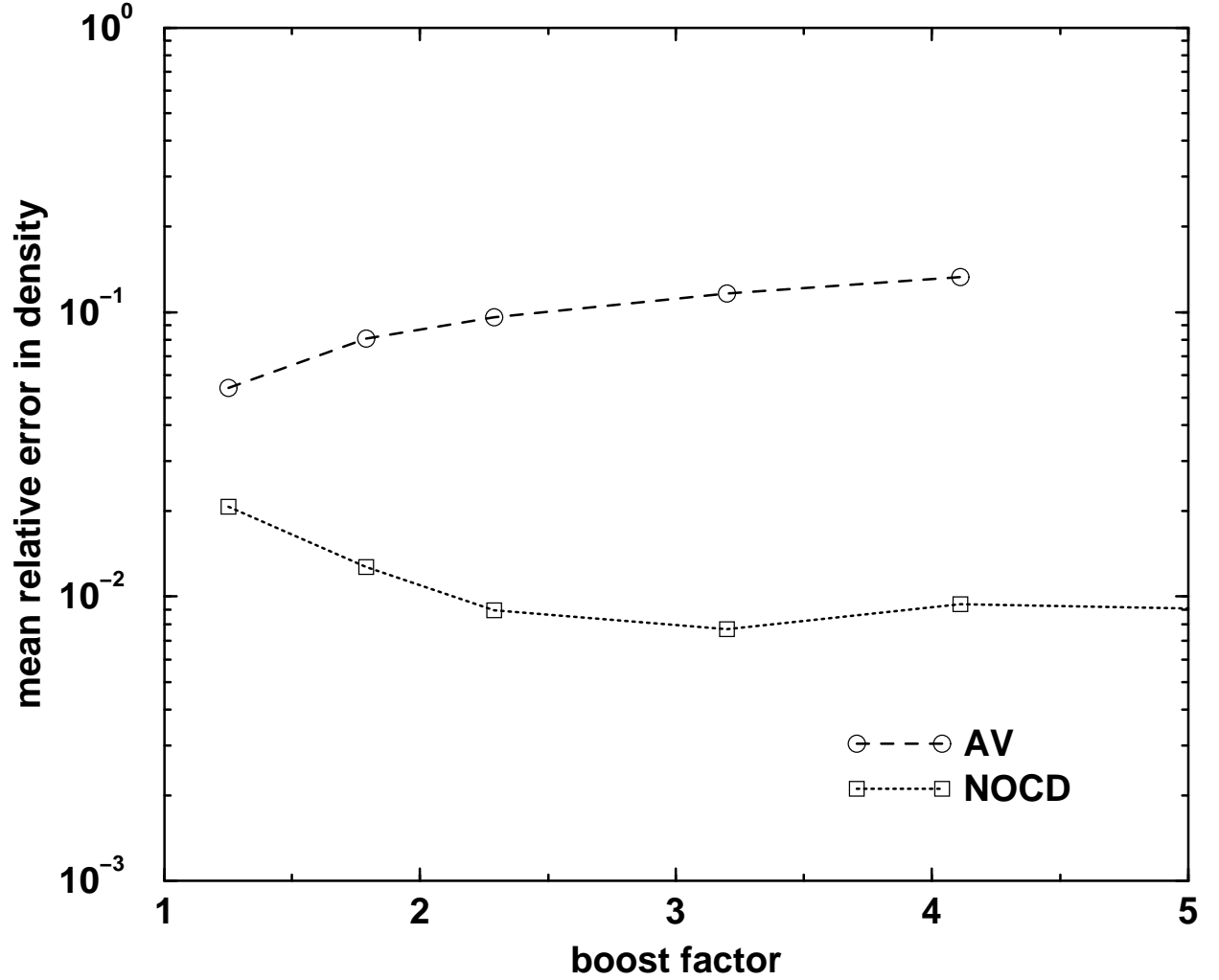


Fig. 8.— Mean relative errors in density for both the AV and NOCD methods as a function of boost for the relativistic wall shock problem. All calculations were run using 200 zones up to time $t = 2.0$. The AV results can be significantly improved and brought closer in alignment with the NOCD results by simply reducing the Courant factor or increasing the viscosity coefficients over the standard values we have chosen for all the tests.

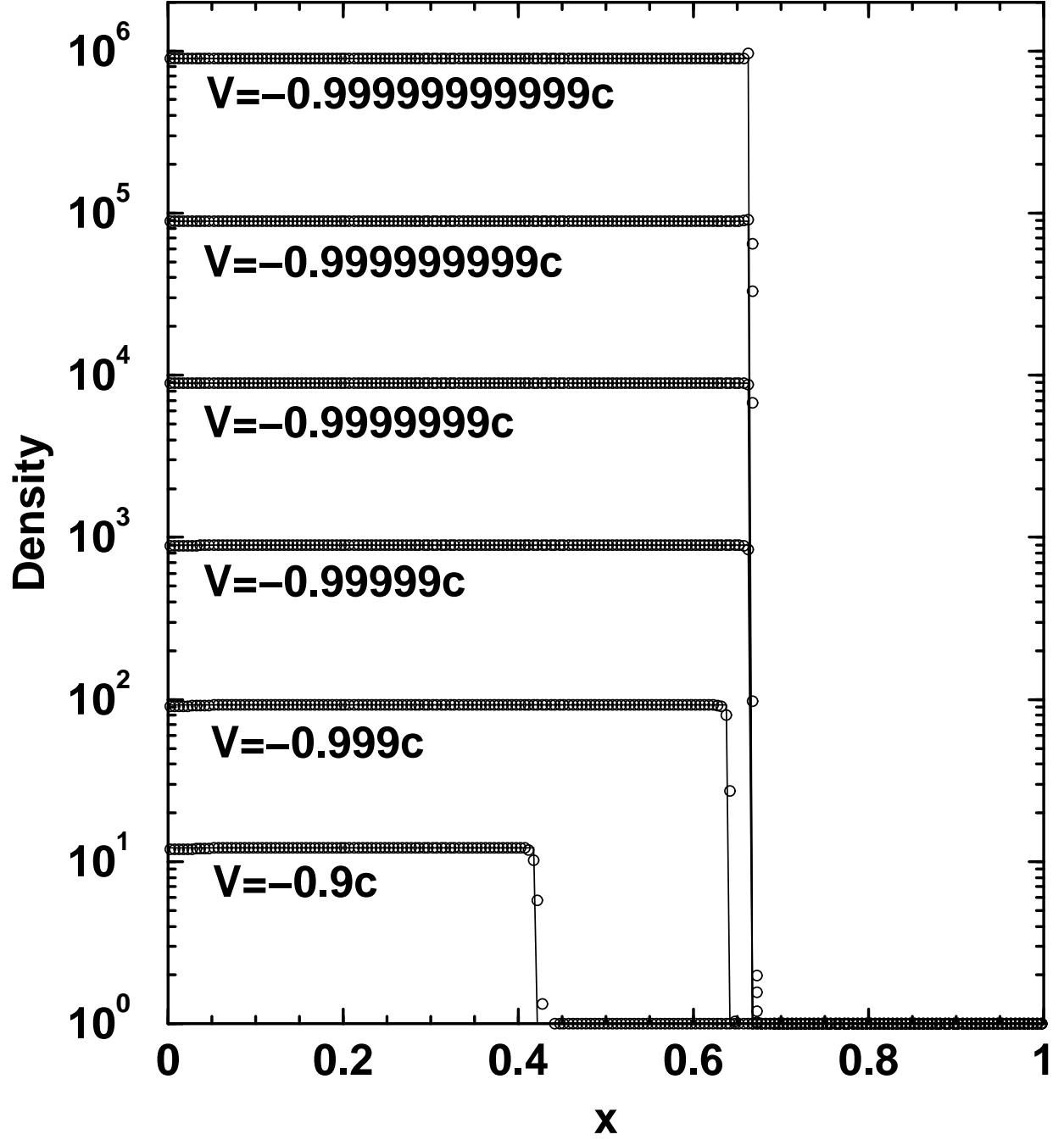


Fig. 9.— Density plots for different infall velocities in the wall shock test using the NOCD method. The resolution is 200 zones and the displayed time is $t = 2.0$.

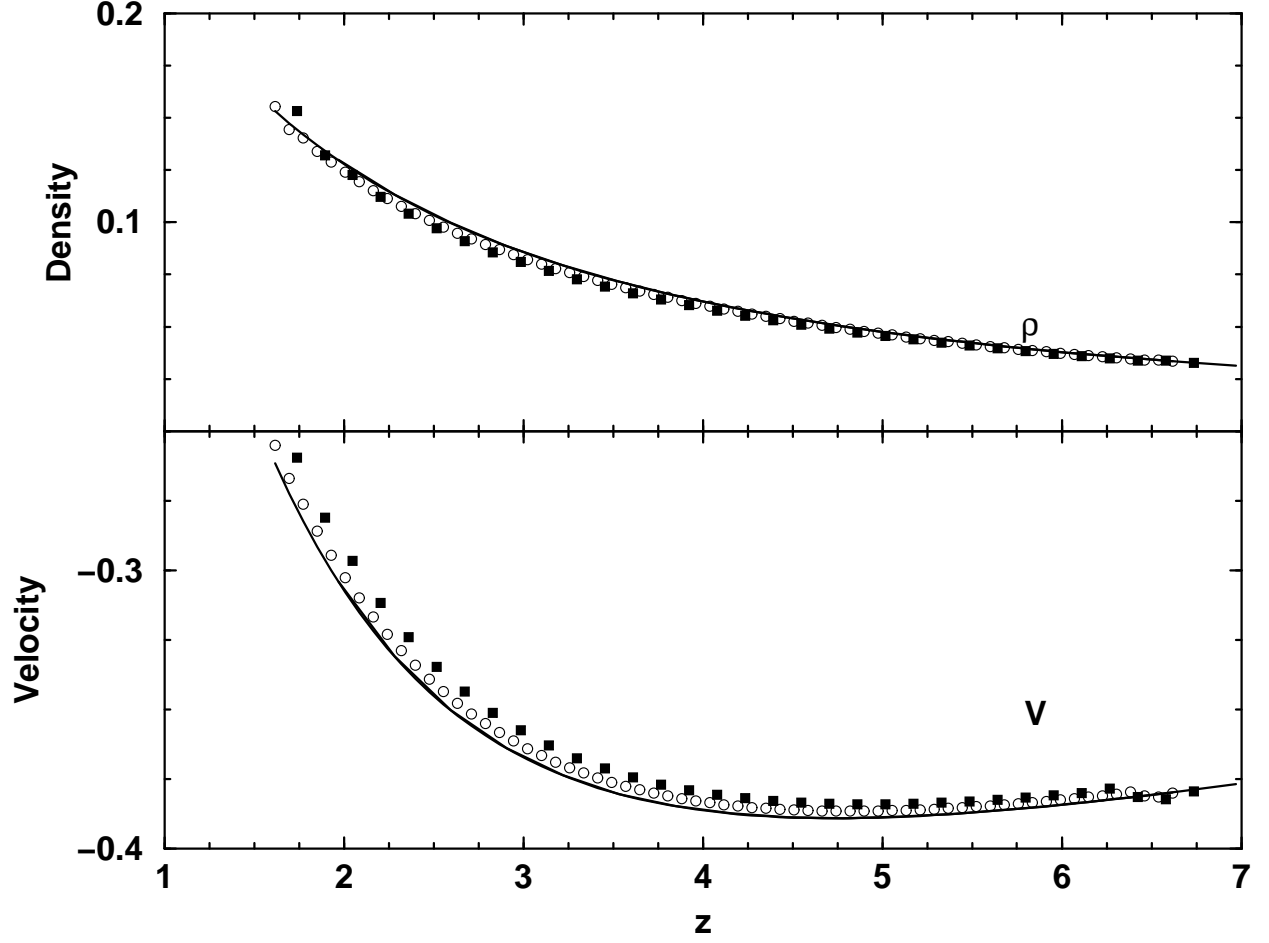


Fig. 10.— Plots of density and velocity along the z -axis for the dust accretion problem using the AV method. The filled squares and open circles correspond to resolutions of 32^3 and 64^3 , respectively. The solid line is the analytic solution. The displayed time is $t = 50M$.

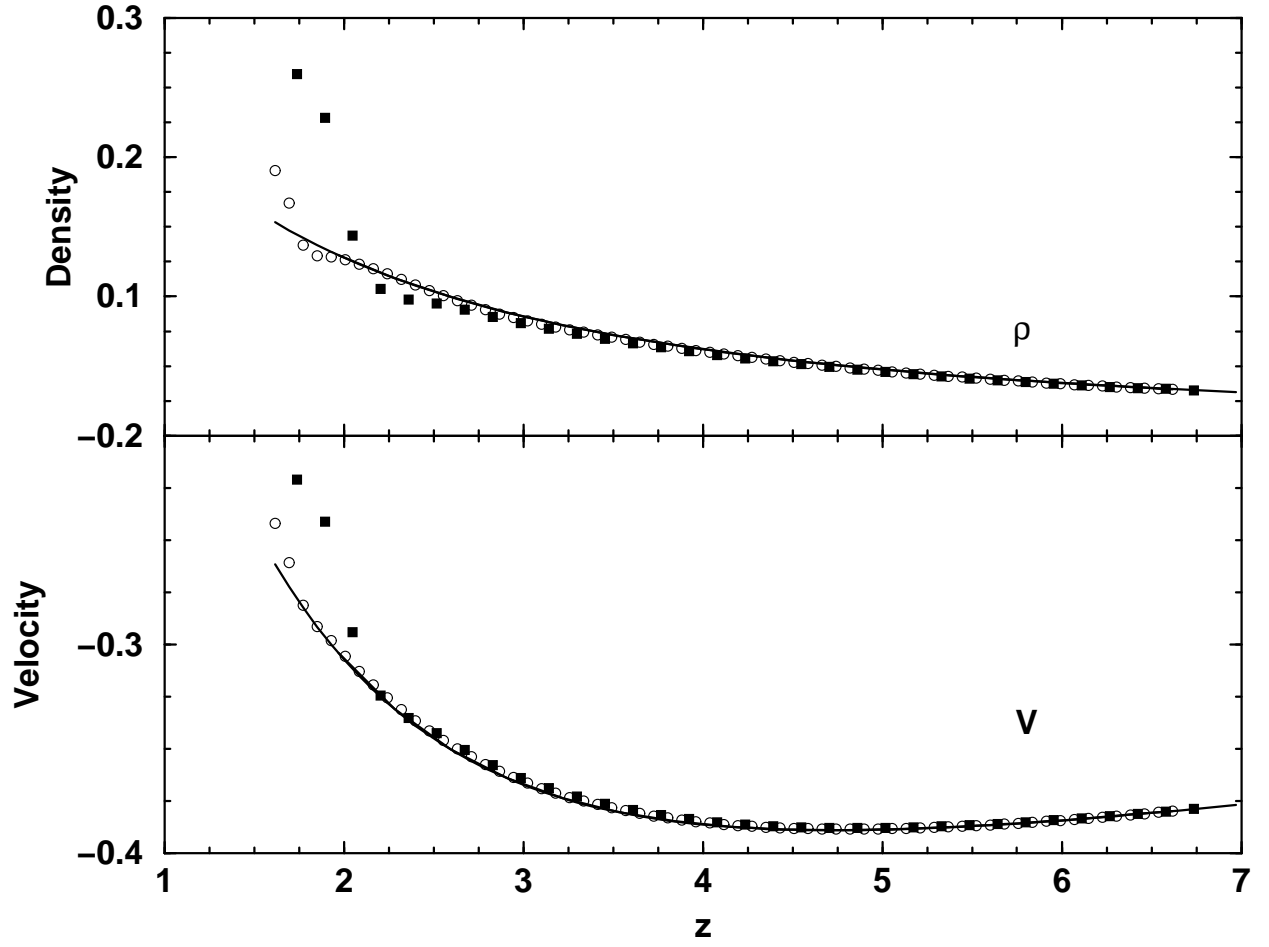


Fig. 11.— As Figure 10, except for the NOCD method.

Grid	Method	$\ E(\rho)\ _1$	$\ E(P)\ _1$	$\ E(V)\ _1$
200	AV	9.08×10^{-2}	5.62×10^{-2}	1.18×10^{-2}
	NOCD	1.06×10^{-1}	5.50×10^{-2}	1.17×10^{-2}
	Marquina ^a	7.65×10^{-2}	4.60×10^{-2}	8.13×10^{-3}
400	AV	4.90×10^{-2}	3.00×10^{-2}	5.59×10^{-3}
	NOCD	4.60×10^{-2}	2.00×10^{-2}	4.13×10^{-3}
	Marquina ^a	4.65×10^{-2}	2.41×10^{-2}	4.84×10^{-3}
800	AV	3.23×10^{-2}	1.86×10^{-2}	3.74×10^{-3}
	NOCD	2.97×10^{-2}	1.35×10^{-2}	2.67×10^{-3}
128 ³	AV	1.43×10^{-1}	1.43×10^{-1}	7.40×10^{-3}
	NOCD	6.36×10^{-2}	6.74×10^{-2}	4.84×10^{-3}
	Marquina ^a	9.23×10^{-2}	7.98×10^{-2}	9.66×10^{-3}

Table 1: L -1 norm errors in density, pressure, and velocity for the moderate boost shock-tube tests.

^aFont et al. (2000)

Grid	Method	$\ E(\rho)\ _1$	$\ E(D)\ _1$	$\ E(P)\ _1$	$\ E(\tau)\ _1$	$\ E(V)\ _1$	$\ E(S)\ _1$
400	AV	1.87×10^{-1}		6.88×10^0		2.20×10^{-2}	
	NOCD	1.85×10^{-1}		5.22×10^0		3.00×10^{-2}	
	PPM ^a		3.21×10^{-1}		4.10×10^0		4.25×10^0
800	AV	1.38×10^{-1}		3.68×10^0		1.24×10^{-2}	
	NOCD	1.28×10^{-1}		2.63×10^0		1.67×10^{-2}	
	PPM ^a		1.78×10^{-1}		2.67×10^0		2.71×10^0
1600	AV	1.00×10^{-1}		2.07×10^0		7.29×10^{-3}	
	NOCD	8.52×10^{-2}		1.68×10^0		8.76×10^{-3}	
	PPM ^a		1.00×10^{-1}		1.89×10^0		1.83×10^0

Table 2: L_1 norm errors in density, pressure, and velocity for the high boost shock-tube tests. Quoted errors for the PPM method represent the conserved quantities, not primitive variables.

^aMartí & Müller (1996)

P_L	Boost	Method	$\bar{\epsilon}_{\text{rel}}(\rho)$	$\bar{\epsilon}_{\text{rel}}(P)$	$\bar{\epsilon}_{\text{rel}}(V)$
1.33	1.08	AV	5.15×10^{-3}	2.99×10^{-3}	2.26×10^{-2}
		NOCD	2.49×10^{-3}	1.62×10^{-3}	7.16×10^{-3}
6.67	1.28	AV	5.55×10^{-3}	3.27×10^{-3}	1.12×10^{-2}
		NOCD	4.04×10^{-3}	2.11×10^{-3}	5.58×10^{-3}
13.3	1.43	AV	6.54×10^{-3}	3.78×10^{-3}	1.08×10^{-2}
		NOCD	6.03×10^{-3}	2.75×10^{-3}	7.74×10^{-3}
26.7	1.63	AV	6.54×10^{-3}	3.60×10^{-3}	8.08×10^{-3}
		NOCD	8.36×10^{-3}	3.38×10^{-3}	8.58×10^{-3}
66.7	1.96	AV	1.48×10^{-2}	6.13×10^{-3}	1.14×10^{-2}
		NOCD	1.39×10^{-2}	5.01×10^{-3}	1.32×10^{-2}
133.3	2.28	AV	2.00×10^{-2}	6.58×10^{-3}	1.31×10^{-2}
		NOCD	1.99×10^{-2}	5.90×10^{-3}	1.70×10^{-2}
266.7	2.66	AV	3.24×10^{-2}	8.22×10^{-3}	1.60×10^{-2}
		NOCD	2.70×10^{-2}	6.91×10^{-3}	2.07×10^{-2}
666.7	3.28	AV	4.37×10^{-2}	1.03×10^{-2}	1.97×10^{-2}
		NOCD	3.62×10^{-2}	8.15×10^{-3}	2.64×10^{-2}
1333.3	3.85	AV	7.77×10^{-2}	3.09×10^{-2}	4.23×10^{-2}
		NOCD	4.33×10^{-2}	9.32×10^{-3}	3.37×10^{-2}

Table 3: Mean-relative errors in the primitive variables for different boost factors in the shock-tube test using an 800 zone grid.

Grid	Method	$\ E(\rho)\ _1$	$\ E(P)\ _1$	$\ E(V)\ _1$
200	AV	$1.56(0.57) \times 10^{-1}$	3.23×10^{-2}	5.48×10^{-3}
	NOCD	$5.10(1.08) \times 10^{-2}$	1.60×10^{-2}	3.34×10^{-3}
400	AV	$1.06(0.29) \times 10^{-1}$	2.18×10^{-2}	2.59×10^{-3}
	NOCD	$3.26(0.48) \times 10^{-2}$	1.10×10^{-2}	2.69×10^{-3}
800	AV	$9.51(1.43) \times 10^{-2}$	2.40×10^{-2}	2.07×10^{-3}
	NOCD	$1.74(0.22) \times 10^{-2}$	6.26×10^{-3}	1.50×10^{-3}

Table 4: L_1 norm errors for the relativistic wall shock test with infall velocity $V = -0.9c$. The values given in parentheses are the contribution of the first 20 zones to the total error. Wall heating dominates and greatly inflates the errors in regions near the reflective boundary, especially in the AV methods.

ν	Method	$\bar{\epsilon}_{\text{rel}}(\rho)$	$\bar{\epsilon}_{\text{rel}}(P)$	$\bar{\epsilon}_{\text{rel}}(V)$
0.4	AV	5.40×10^{-2}	4.71×10^{-2}	6.33×10^{-3}
	NOCD	2.07×10^{-2}	2.48×10^{-2}	9.91×10^{-3}
	Wilson ^a	5.36×10^{-2}		
0.17	AV	8.09×10^{-2}	6.42×10^{-2}	2.14×10^{-2}
	NOCD	1.27×10^{-2}	1.15×10^{-2}	9.31×10^{-3}
	Wilson ^a	6.98×10^{-2}		
0.1	AV	9.59×10^{-2}	7.44×10^{-2}	3.66×10^{-2}
	NOCD	8.95×10^{-3}	7.23×10^{-3}	6.41×10^{-3}
	Wilson ^a	8.29×10^{-2}		
	Marquina ^b	9.66×10^{-3}	9.07×10^{-3}	8.03×10^{-3}
0.05	AV	1.16×10^{-1}	8.51×10^{-2}	5.76×10^{-2}
	NOCD	7.69×10^{-3}	6.12×10^{-3}	6.74×10^{-3}
0.03	AV	1.33×10^{-1}	9.38×10^{-2}	7.38×10^{-2}
	NOCD	9.40×10^{-3}	7.25×10^{-3}	1.01×10^{-2}
10^{-3}	NOCD	4.43×10^{-3}	2.73×10^{-3}	4.60×10^{-3}
	Marquina ^b	7.20×10^{-3}	5.80×10^{-3}	1.26×10^{-2}
10^{-5}	NOCD	2.09×10^{-3}	1.01×10^{-3}	1.35×10^{-3}
	Marquina ^b	7.93×10^{-3}	1.00×10^{-3}	7.20×10^{-3}
10^{-7}	NOCD	6.30×10^{-3}	5.59×10^{-3}	1.29×10^{-2}
	Marquina ^b	9.30×10^{-3}	6.10×10^{-3}	8.56×10^{-3}
10^{-9}	NOCD	5.82×10^{-3}	5.14×10^{-3}	9.97×10^{-3}
	Marquina ^b	1.03×10^{-2}	6.52×10^{-3}	8.13×10^{-3}
10^{-11}	NOCD	1.12×10^{-3}	8.27×10^{-4}	5.08×10^{-4}
	Marquina ^b	3.40×10^{-2}	1.41×10^{-3}	3.26×10^{-3}

Table 5: Mean-relative errors in density, pressure, and velocity over a broad range of infall velocities ($|V| = 1 - \nu$) in the wall shock test using a 200 zone grid. As noted in the text, the AV errors can be reduced significantly and brought closer in agreement with the NOCD results by either increasing the viscosity strength or decreasing the Courant factor.

^aCentrella & Wilson (1984)

^bAloy, Ibáñez, & Martí (1999)

Grid	Method	$\bar{\epsilon}_{\text{rel}}(\rho)$	$\bar{\epsilon}_{\text{rel}}(V)$
16^3	AV	4.81×10^{-2}	3.08×10^{-2}
	NOCD	1.01×10^{-1}	1.53×10^{-2}
32^3	AV	2.70×10^{-2}	1.34×10^{-2}
	NOCD	4.55×10^{-2}	3.26×10^{-3}
64^3	AV	1.36×10^{-2}	6.32×10^{-3}
	NOCD	2.11×10^{-2}	1.44×10^{-3}

Table 6: Mean-relative errors in density and velocity for the black hole accretion problem at time $t = 50M$, where $M = 1$ is the black hole mass.